NASA/TM—2004-212625

Effect of Sintering on Mechanical and Physical Properties of Plasma-Sprayed Thermal Barrier Coatings

Sung R. Choi
Ohio Aerospace Institute, Brook Park, Ohio

Dongming Zhu
U.S. Army Research Laboratory, Glenn Research Center, Cleveland, Ohio

Robert A. Miller
Glenn Research Center, Cleveland, Ohio

April 2004

The NASA STI Program Office . . . in Profile

Since its founding, NASA has been dedicated to the advancement of aeronautics and space science. The NASA Scientific and Technical Information (STI) Program Office plays a key part in helping NASA maintain this important role.

The NASA STI Program Office is operated by Langley Research Center, the Lead Center for NASA's scientific and technical information. The NASA STI Program Office provides access to the NASA STI Database, the largest collection of aeronautical and space science STI in the world. The Program Office is also NASA's institutional mechanism for disseminating the results of its research and development activities. These results are published by NASA in the NASA STI Report Series, which includes the following report types:

- TECHNICAL PUBLICATION. Reports of completed research or a major significant phase of research that present the results of NASA programs and include extensive data or theoretical analysis. Includes compilations of significant scientific and technical data and information deemed to be of continuing reference value. NASA's counterpart of peer-reviewed formal professional papers but has less stringent limitations on manuscript length and extent of graphic presentations.

- TECHNICAL MEMORANDUM. Scientific and technical findings that are preliminary or of specialized interest, e.g., quick release reports, working papers, and bibliographies that contain minimal annotation. Does not contain extensive analysis.

- CONTRACTOR REPORT. Scientific and technical findings by NASA-sponsored contractors and grantees.

- CONFERENCE PUBLICATION. Collected papers from scientific and technical conferences, symposia, seminars, or other meetings sponsored or cosponsored by NASA.

- SPECIAL PUBLICATION. Scientific, technical, or historical information from NASA programs, projects, and missions, often concerned with subjects having substantial public interest.

- TECHNICAL TRANSLATION. English-language translations of foreign scientific and technical material pertinent to NASA's mission.

Specialized services that complement the STI Program Office's diverse offerings include creating custom thesauri, building customized databases, organizing and publishing research results . . . even providing videos.

For more information about the NASA STI Program Office, see the following:

- Access the NASA STI Program Home Page at ***http://www.sti.nasa.gov***

- E-mail your question via the Internet to help@sti.nasa.gov

- Fax your question to the NASA Access Help Desk at 301–621–0134

- Telephone the NASA Access Help Desk at 301–621–0390

- Write to:
  NASA Access Help Desk
  NASA Center for AeroSpace Information
  7121 Standard Drive
  Hanover, MD 21076

NASA/TM—2004-212625

Effect of Sintering on Mechanical and Physical Properties of Plasma-Sprayed Thermal Barrier Coatings

Sung R. Choi
Ohio Aerospace Institute, Brook Park, Ohio

Dongming Zhu
U.S. Army Research Laboratory, Glenn Research Center, Cleveland, Ohio

Robert A. Miller
Glenn Research Center, Cleveland, Ohio

National Aeronautics and
Space Administration

Glenn Research Center

April 2004

Acknowledgments

The authors are grateful to both Ralph Pawlik for the experimental work and George Leissler for processing TBC billets. This work was supported by the Ultra-Efficient Engine Technology (UEET) program, NASA Glenn Research Center, Cleveland, Ohio.

Available from

NASA Center for Aerospace Information
7121 Standard Drive
Hanover, MD 21076

National Technical Information Service
5285 Port Royal Road
Springfield, VA 22100

Available electronically at http://gltrs.grc.nasa.gov

Effect of Sintering on Mechanical and Physical Properties of Plasma-Sprayed Thermal Barrier Coatings

Sung R. Choi
Ohio Aerospace Institute
Brook Park, Ohio 44142

Dongming Zhu
U.S. Army Research Laboratory
Glenn Research Center
Cleveland, Ohio 44135

Robert A. Miller
National Aeronautics and Space Administration
Glenn Research Center
Cleveland, Ohio 44135

Summary

The effect of sintering on mechanical and physical properties of free-standing plasma-sprayed ZrO_2-8 wt% Y_2O_3 thermal barrier coatings (TBCs) was determined by annealing them at 1316 °C in air. Mechanical and physical properties of the TBCs, including strength, modes I and II fracture toughness, elastic modulus, Poisson's response, density, microhardness, fractography, and phase stability, were determined at ambient temperature as a function of annealing time ranging from 0 to 500 h. All mechanical and physical properties, except for the amount of monoclinic phase, increased significantly in 5 to 100 h and then reached a plateau above 100 h. Annealing resulted in healing of microcracks and pores and in grain growth, accompanying densification of the TBC's body due to the sintering effect. However, an inevitable adverse effect also occurred such that the desired lower thermal conductivity and good expansivity, which makes the TBCs unique in thermal barrier applications, were degraded upon annealing. A model was proposed to assess and quantify all the property variables in response to annealing in a normalized scheme. Directionality of as-sprayed TBCs appeared to have an insignificant effect on their properties, as determined via fracture toughness, microhardness, and elastic modulus measurements.

Introduction

Thermal barrier coatings (TBCs) have attracted ever-increasing attention for advanced gas turbine and diesel engine applications because of their ability to provide thermal insulation to engine components (refs. 1 to 3). The merits of using ceramic TBCs are well recognized and include a potential increase in engine operating temperature with reduced cooling requirements, resulting in significant improvements in thermal efficiency, performance, and reliability. Plasma-sprayed zirconia-based ceramics are one of the most important coating materials in light of their low thermal conductivity, relatively high thermal expansivity, and unique microstructure as a result of plasma spraying process. However, the durability of TBCs under severe thermal and mechanical loading conditions encountered in heat engines remains one of the major problems. As a result, the development of TBCs requires better understanding of both mechanical and thermal behavior of the coating materials to ensure life and reliability of the related components.

Because of their unique application process, plasma-sprayed TBCs exhibit a complicated but unique microstructure with numerous macro- and microcracks, porosity, and lamellarlike splat morphology. As a result, plasma-sprayed TBCs, when heated to elevated temperatures, have exhibited a sintering effect through crack healing, inter- and/or transsplat bonding, and grain growth with their degree of sintering depending on heating temperature and time (refs. 4 to 8). The sintering effect has been well known to change mechanical and physical properties of TBCs through the processes mentioned above. It has been shown that elastic modulus (refs. 4 to 8), strength (refs. 4 and 5), and work of fracture (ref. 5) of as-sprayed TBCs all increased upon annealing at elevated temperatures. Thermal conductivity has been shown to increase as well (refs. 4 and 6). Sintering could result in an increase in mechanical properties but at the same time deteriorate thermal conductivity and strain tolerance (expansivity), thereby degrading the important feature of the coatings as a thermal barrier.

Therefore, it is important to quantify the effect of sintering on mechanical and physical properties of TBCs to ensure reliability and life of the components in service conditions. Various efforts have been concentrated primarily to determine one or two mechanical properties (such as modulus and/or strength) although a recent study by Thurn et al. (ref. 5) expanded more to include elastic modulus, strength, and work of fracture. No systematic sintering study, aimed at a particular service temperature as a function of time from the same batch of TBCs, has been done to include all possible mechanical and physical properties such as strength, fracture toughness, elastic modulus, microhardness, deformation, thermal conductivity, phase stability, etc. This work, as a consequence, was focused on determining as completely and systematically as possible the effect of sintering on mechanical and physical properties of plasma-sprayed free-standing thick TBCs that were from the same batch of the material. Test coupons of as-sprayed TBCs, with their specimen configurations depending on test matrix, were first annealed at 1316 °C in air as a function of time ranging from 0 to 500 h, and their respective properties were then determined at ambient temperature. The properties thus determined included flexure strength, mode I and mode II fracture toughnesses (K_{Ic} and K_{IIc}), elastic modulus, Poisson's response, density, microhardness, and phase stability. The annealing temperature chosen in this work was one of the target service temperatures from the ongoing advanced aeroengine programs at NASA Glenn. A generalized, phenomenological model is proposed and discussed to better quantify mechanical and physical responses of TBCs to sintering.

Experimental Procedures

Material

ZrO_2-8 wt% Y_2O_3 powder with an average particle size of 60 μm was first plasma sprayed onto a rectangular graphite substrate measuring 150 by 100 by 6.5 mm to a thickness of about 6 mm, using a Sulzer-Metco ATC–1 plasma coating system (Sulzer Metco, Inc., Westbury, NY) with an industrial robot. The plasma-spray conditions can be found elsewhere (ref. 9). A freestanding, plasma-sprayed ceramic billet was then obtained by slowly burning out the graphite substrate at 680 °C in air for 24 h. The billets were machined into the configurations of test specimens with a final finish using a #500 diamond grinding wheel according to the test matrix described below. Two test-specimen configurations machined from billets showing their orientation relative to plasma-spray direction are depicted in figure 1. Previously determined mechanical and physical properties of interest of the as-sprayed coating material at ambient temperature are presented in table I (refs. 10 to 15). Figure 2 shows polished surfaces displaying (a) lamellae, (b) microcracks and pores, and (c) a fracture surface revealing unique platelet structure.

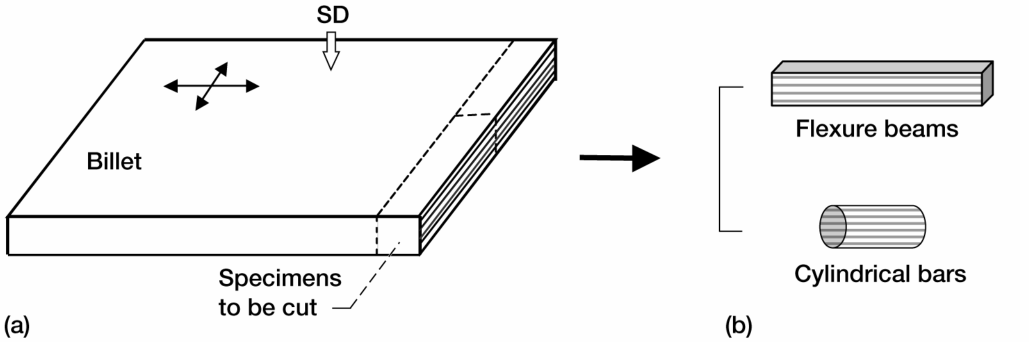

Figure 1.—Billet and test specimen configurations. (a) Billet showing plasma-spray direction (SD) with specimens to be cut. (b) Test specimen configurations of flexure beams and cylindrical bars machined from billet. Layers are indicated.

TABLE I.—MECHANICAL AND PHYSICAL PROPERTIES OF PLASMA-SPRAYED ZrO_2-8 WT% Y_2O_3 THERMAL BARRIER COATINGS AT AMBIENT TEMPERATURE
[From refs. 10 to 15]

Density, ρ, g/cm^3	Elastic modulus, E, GPa	Fracture toughness,[a] MPa $\sqrt{m}$		Strength		
		Mode I, K_{Ic}	Mode II, K_{IIc}	Type of test	Number of specimens	Average strength,[a] MPa
5.22	34	1.2(0.1)	0.7(0.1)	Tension	10	10 (2)
				Transthickness tension	10	11(1)
				Compression	10	324(72)
				Four-point flexure	20	32(6)
				Biaxial flexure	10	40(4)

[a] Numbers in parentheses represent ±1.0 standard deviation.

Annealing and Mechanical Testing

Annealing.—Annealing (often called “sintering” in the TBCs community) was conducted at 1316 °C in air using either cylindrical bar or rectangular flexure beam specimen configuration depending on the type of testing. Test specimens were heated with a heating rate of about 20 °C/min, held for a specified annealing time, and then furnace cooled. After annealing, each of the mechanical or physical properties was determined as a function of annealing time in accordance with procedures described below. Typically, a total of five different annealing times of 0, 5, 20, 100, and 500 h were employed for a given property evaluation.

Flexure strength.—Flexure test specimens (see fig. 3(a)) measuring 4, 3, and 25 mm, respectively, in width, depth, and length were annealed at 1316 °C in air for 0, 5, 20, 100, and 500 h. A total of 5 to 10 specimens were annealed at each duration. The corresponding strength of annealed test specimens was determined at ambient temperature in four-point flexure with 10-mm inner and 20-mm outer spans using an actuator speed of 0.0083 mm/s in an electromechanical test frame (Model 8562, Instron, Canton, MA). One of two 4-mm-wide faces of each test specimen that was perpendicular to the plasma-spray direction was subjected to tension in flexure loading. The coatings have exhibited negligible slow crack growth at either ambient or elevated (800 °C) temperature with slow-crack-growth parameter n greater than 100 (refs. 10 and 13); hence, the test rate used here, 0.0083 mm/s, was considered sufficiently fast to minimize

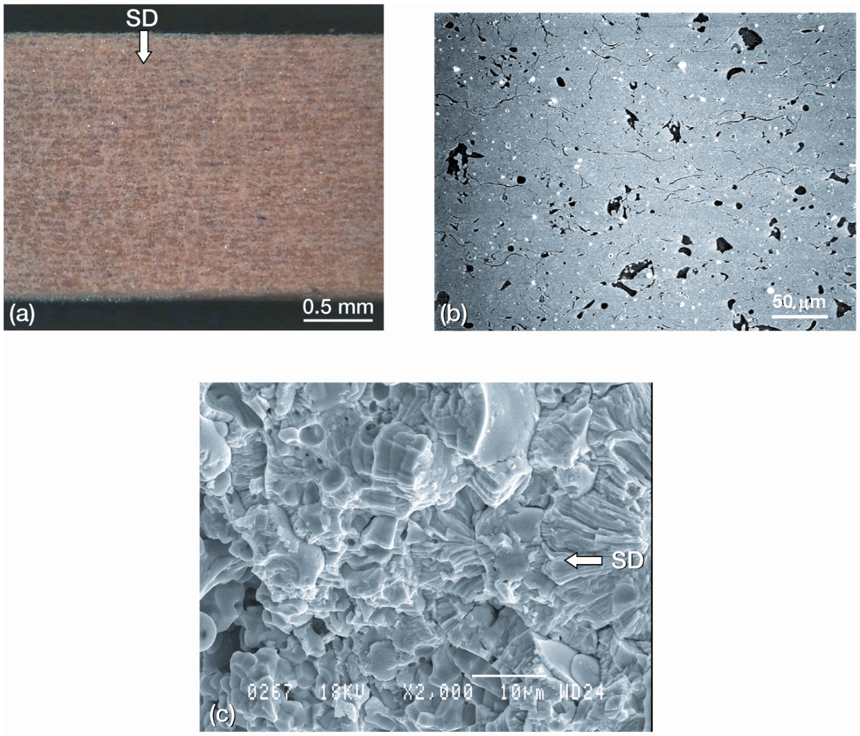

Figure 2.—Typical microstructures of plasma-sprayed ZrO_2-8 wt% Y_2O_3 thermal barrier coatings. Arrows indicate plasma-spray direction (SD). (a) Side view of flexure specimen showing lamellae (layers). (b) Polished top surface. (c) Fracture surface.

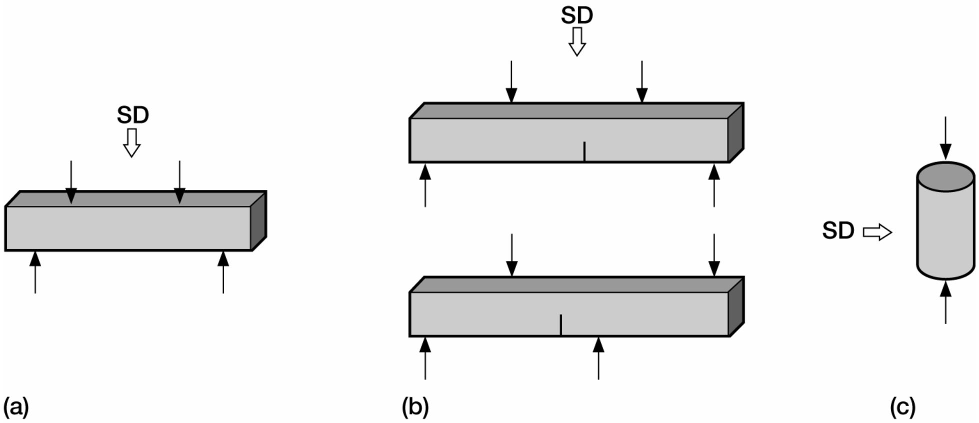

Figure 3.—Three representative test specimens and loading configurations of plasma-sprayed ZrO_2-8 wt% Y_2O_3 thermal barrier coatings used in this work. Open arrows indicate plasma-spray direction (SD). (a) Four-point-flexure specimen for flexure strength tests. (b) Symmetric and asymmetric four-point-flexure specimens for modes I and II fracture toughness tests. (c) Cylindrical rod specimen in compression for elastic modulus and constitutive relations tests.

slow crack growth effects during strength testing. Flexure testing and specimen preparation, in general, were in accordance with ASTM C1611 (ref. 16).

Modes I and II fracture toughness (K_{Ic} and K_{IIc}).—Flexure test specimens with measurements of 3 and 4 mm in width and depth and a measurement of either 25 or 50 mm in length were used for determination of modes I and II fracture toughnesses (K_{Ic} and K_{IIc}) after annealing for 0, 5, 10, 20, and 500 h. For each mode of fracture toughness, a total of four to five test coupons were used at each annealing time and then fracture-toughness tested at ambient temperature, as stated below.

Sharp V notches were introduced in test specimens using the single-edge-V-notched-beam (SEVNB) method (ref. 17). This method utilizes a razor blade with diamond paste to introduce a sharp root radius by tapering a saw cut. A starter straight-through notch about 1.2 mm deep and 0.026 mm wide was made on the 3-mm-wide face of test coupons. The final notch depth and root radius were finished with a steel razor blade with diamond paste to be about 2.0 mm and 20 to 50 µm, respectively. Details of this procedure can be found elsewhere (refs. 10 and 17). The coating material had less sharpness in its root radius compared with typical dense ceramics because of its porous and microcracked nature. However, it has been observed that the sharpness ranging from 20 to 50 µm is sufficient to give a consistent and accurate value of fracture toughness of the coating material (refs. 10 and 14). Note that the through-the-thickness sharp notches thus prepared were aligned toward the plasma-spray direction (see fig. 3(b)). Other methods to generate sharp cracks to estimate fracture toughness are not feasible for these coatings. The indentation response is so poor—precracks were neither controllable in size nor easily discernable in the crack front from fracture surfaces—so that the single-edge-precracked-beam (SEPB) (ref. 18) and other indentation techniques are not testing options. This poor indentation response is attributed to the material’s significant porosity, microcracks, and softness compared with other structural ceramics.

In mode I fracture toughness testing, each test specimen with a sharp V notch located at its center was loaded in symmetric four-point flexure with 10-mm inner and 20-mm outer spans for the 25-mm-long test specimens or with 20-mm inner and 40-mm outer spans for the 50-mm-long test specimens (see fig. 3(b)). In mode II testing, the sharp V-notched test specimens were loaded in asymmetric four-point flexure as shown in figure 4. The precrack was centered with respect to the loading point (s = 0) so that the precrack

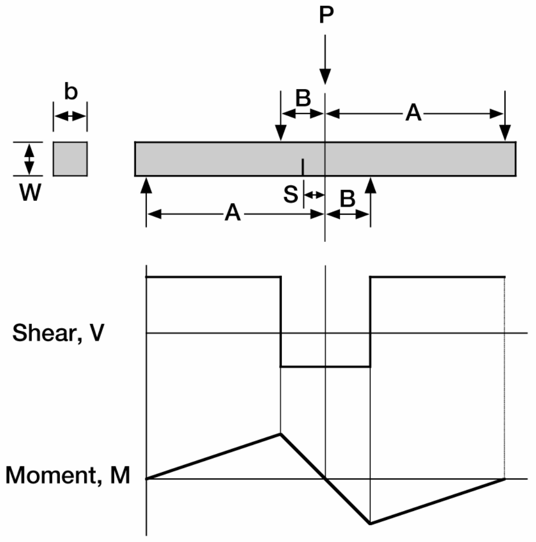

Figure 4.—Schematics of asymmetric four-point-flexure specimen geometry with accompanying shear force and bending moment diagrams used in mode II fracture toughness (K_{IIc}) testing for plasma-sprayed ZrO_2-8 wt% Y_2O_3 thermal barrier coatings.

was subjected to pure mode II loading. Of course, the ratio of mode I to mode II loading can be varied by varying the distance of the precrack from the center plane, *s*, as previously done for mixed-mode fracture behavior of TBCs at both 25 and 1316 °C (ref. 14). The values of A = 10 mm and B = 5 mm were used in mode II fracture toughness testing. Both modes I and II fracture toughness tests were conducted at ambient temperature in air using the same actuator speed (0.0083 mm/s) and test frame that were used in flexure strength testing. After testing, the crack size of each specimen tested was determined optically from its fracture surface based on the three-point measurements in accordance with the test standard ASTM C1421 (ref. 18). Fracture toughnesses K_{Ic} and K_{IIc} were calculated using the following relations:

$$K_{\mathrm{I}} = \sigma(\pi a)^{1/2} F_{\mathrm{I}}\left(\frac{a}{W}\right) \tag{1}$$

$$K_{\mathrm{II}} = \tau(\pi a)^{1/2} F_{\mathrm{II}}\left(\frac{a}{W}\right) \tag{2}$$

where σ is the applied (remote) normal stress, τ is the applied (remote) shear stress, a is the crack size, and W is the specimen depth (4 mm). F_{I} and F_{II} are crack geometry factors in modes I and II, respectively. The shear stress in pure mode II is given from the elementary beam theory by

$$\tau = \frac{A-B}{A+B}\,\frac{P}{bW} \tag{3}$$

where b is the specimen width (3 mm), and P is the applied force. Several different expressions of F_{II} were suggested by Suresh et al. (ref. 19), Wang et al. (ref. 20), and He et al. (ref. 21) for the case of a through-the-thickness crack, and their respective results of F_{II} do not yield any significant difference, particularly when a/W = 0.35 to 0.50. The solution by He et al. (ref. 21), which provides a convenient polynomial expression, is used here as follows:

$$F_{\mathrm{II}}\left(\frac{a}{W}\right) = 7.264 - 9.37\left(\frac{a}{W}\right) + 2.74\left(\frac{a}{W}\right)^2 + 1.87\left(\frac{a}{W}\right)^3 - 1.04\left(\frac{a}{W}\right)^4 \quad \text{for } 0 \le \frac{a}{W} \le 1 \tag{4}$$

The solution for F_{I} is taken from Murakami (ref. 22), which is almost identical to the Srawly and Gross solution (ref. 23) for $a/W \le 0.7$:

$$F_{\mathrm{I}}\left(\frac{a}{W}\right) = 1.122 - 1.121\left(\frac{a}{W}\right) + 3.740\left(\frac{a}{W}\right)^2 + 3.873\left(\frac{a}{W}\right)^3 - 19.05\left(\frac{a}{W}\right)^4 + 22.55\left(\frac{a}{W}\right)^5 \tag{5}$$

Elastic modulus.—Cylindrical rod test specimens (see fig. 3(c)) were used to determine the elastic modulus in compression as a function of annealing time. The nominal dimensions of test specimens were 5 and 10 mm, respectively, in diameter and length. The plasma-spraying direction was normal to the specimen's longitudinal axis. Five different annealing times t = 0, 5, 20, 100, and 500 h were used. Two specimens were annealed at each specified time. After annealing, each test specimen was strain gaged and subjected to a monotonic loading and unloading cycle in compression to its longitudinal direction. A maximum compression load of 900 N (46 MPa) was applied using a specially designed test fixture. Resultant load-strain curves were obtained, and the elastic modulus was determined from their slopes. In some cases, biaxial strain gages were used to determine both longitudinal and lateral strain components from which Poisson's response would be determined. The test frame was the same as that used in flexure strength and fracture toughness testing.

The impulse excitation method was also used to determine elastic modulus of annealed flexure test specimens measuring 4 by 3 by 50 mm in width, depth, and length, respectively, in accordance with ASTM C1259 (ref. 24). Although this method is primarily for dense materials, this technique was used to find its applicability for porous, less dense TBCs and to compare with the strain gage method. Two flexure test specimens were continuously used throughout testing such that each individual elastic modulus was determined at each of the five annealing times, from $t = 0$ to 500 h. Impulse excitation was applied to the 4-mm-wide face of each flexure beam specimen, where the direction of vibration of a beam was parallel to the plasma-spray direction (or normal to the lamellae). At each step of elastic modulus measurements, density was subsequently determined at the corresponding annealing time using the mass-volume method.

Microhardness, fractography, and phase stability.—Vickers microhardness was determined at ambient temperature with remaining specimen halves from mode I fracture toughness testing, chosen at different annealing times of 0, 5, 100, and 500 h. The flexure halves, measuring approximately 3 by 4 by 10 mm, were mounted, and the 4-mm-wide face of each piece was mirror polished. Two indentation loads P_i of 9.8 and 19.6 N were applied using a type 3212 Zwick indenter (Zwick Roell AG, Ulm, Germany) on the polished surface that was parallel to the plasma-spray direction. In general there were five indents made at each load for a given specimen annealed for a given time. Additional tests were also performed at 9.8 N to see variation in microhardness with respect to location within the 4-mm-wide side of a flexure bar specimen annealed for 100 h. The test procedure for hardness measurements was followed in accordance with ASTM C1327 (ref. 25).

Fracture surfaces and polished surface morphologies of test specimens were characterized as a function of annealing time using optical microscopy and scanning electron microscopy (SEM).

The change in the amount of monoclinic phase was also determined as a function of annealing time by x-ray diffraction (XRD) using remaining specimens broken in the mode I fracture toughness testing.

Directionality of as-sprayed TBCs.—TBCs were fabricated via plasma-spray process so that anisotropy would be *microscopically* inevitable due to the prevailing splat structure, preferably aligned with respect to the spraying direction (see fig. 2). As a consequence, plasma-sprayed TBCs would be expected to exhibit anisotropy in their mechanical and/or physical properties. To verify this notion, directionality of as-sprayed TBCs was examined using flexure test specimens by determining both mode I fracture toughness and microhardness as a function of material axis, as shown in figure 5. Fracture toughness in direction 2 was determined by the SEVNB method, whereas fracture toughness in direction 3 (i.e., the interlaminar direction) was determined by the double cantilever beam (DCB) method with a sharp V notch introduced in the midplane of the test specimens. Four to five flexure test specimens were tested in each direction. Fracture toughness in the DCB specimens was calculated based on the formula by Murakami (ref. 22).

Knoop microhardness, in accordance with ASTM C 1326 (ref. 26), was determined with a flexure test specimen at both 0 and 90° on its top (perpendicular to plasma-spraying direction) and side (parallel to plasma-spraying direction) surfaces, as shown in figure 5. A P_i of 9.8 N was used with a total of five indents at each orientation for a given specimen surface. This technique has been used to examine the directionality effect of rolled sheet metals with respect to rolling direction. Additionally, Vickers microhardness with a P_i of 9.8 N was also determined to examine the directionality effect from both top and side surfaces of the specimen that was used in Knoop indentation testing.

Elastic modulus by impulse excitation was also determined in direction 2 (see fig. 5(a) for orientation) using the same as-sprayed flexure test specimens that were used in elastic modulus measurements in direction 1 (see the foregoing section “Elastic Modulus”). In these tests, the direction of vibration of a beam excited by impulse was normal to the plasma-spray direction of vibration. A total of three test specimens were used.

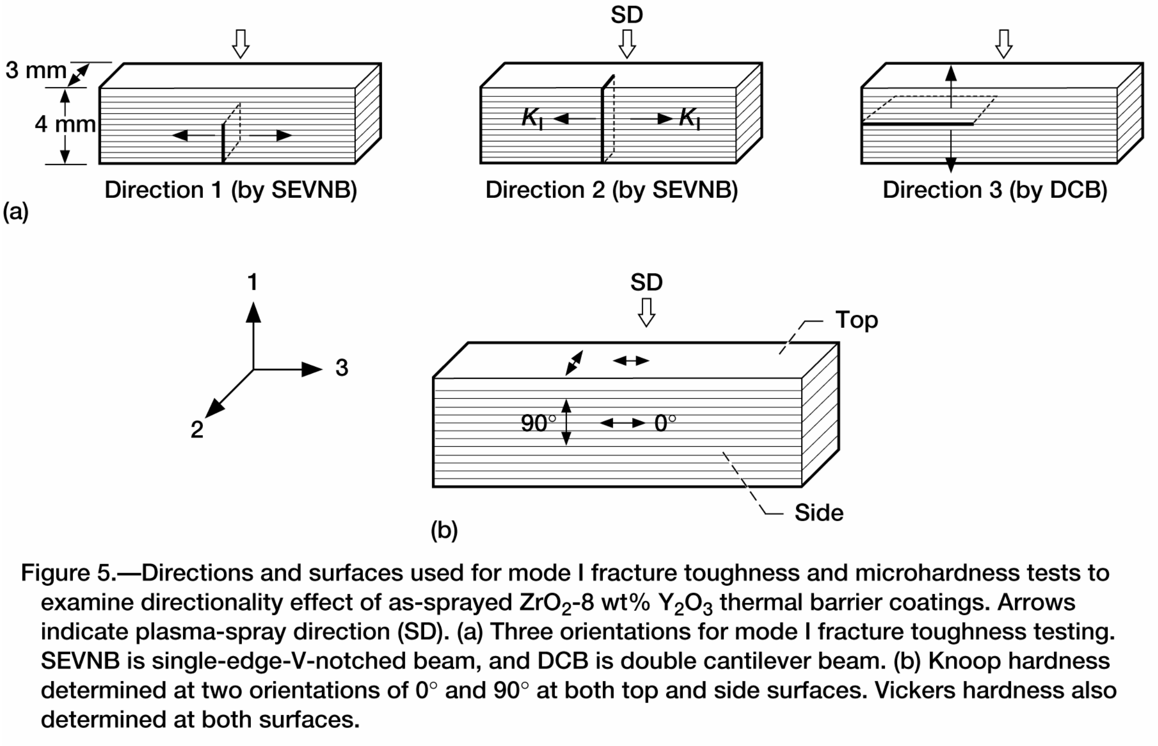

Figure 5.—Directions and surfaces used for mode I fracture toughness and microhardness tests to examine directionality effect of as-sprayed ZrO_2-8 wt% Y_2O_3 thermal barrier coatings. Arrows indicate plasma-spray direction (SD). (a) Three orientations for mode I fracture toughness testing. SEVNB is single-edge-V-notched beam, and DCB is double cantilever beam. (b) Knoop hardness determined at two orientations of 0° and 90° at both top and side surfaces. Vickers hardness also determined at both surfaces.

Results and Discussion

Flexure Strength

The results of flexure strength as a function of annealing time are presented in figure 6. The increase in flexure strength upon annealing was significant, occurring in a short period of time of $t = 20$ h. Flexure strength reached a plateau at $t \geq 20$ h with an approximated value of $\sigma_f = 85$ MPa, about a 130-percent increase from $\sigma_f = 37\pm4$ MPa at $t = 0$ h. Despite the limited number of test specimens (five at each annealing time) used in this work, the results showed a clear trend in strength upon annealing with a steady-state condition occurring within 100 h. However, the flexure strength (85 MPa) of TBCs annealed up to 500 h was still much lower than that (270 MPa) of hot-pressed 10 mol% yttria-stabilized zirconia (YSZ) at ambient temperature (ref. 27). This indicates that the basic open structure inherent in TBCs remained mostly unchanged, even after annealing 500 h, never reaching a dense structure equivalent to the hot-pressed YSZ counterpart. Details regarding microstructural changes of TBCs upon annealing will be described later in the section “Surface Structure and Fractography.” The type of strength-controlled flaws, fracture origins, and their natures were barely able to be determined from fracture surfaces because of problems associated with the open, porous, microcracked, and splat structure of TBCs in either as-sprayed or annealed condition. Because of this, fractography in plasma-sprayed TBC material—unlike in dense ceramics—is an enormous challenge (refs. 13 and 15).

Modes I and II Fracture Toughness

Figure 7 shows the results of modes I and II fracture toughness testing for TBCs annealed at 1316 °C in air. Modes I and II fracture toughness of as-sprayed TBCs, $K_{Ic} = 1.15\pm0.07$ MPa$\sqrt{m}$ and $K_{IIc} = 0.73\pm0.10$ MPa$\sqrt{m}$ (ref. 14), were also included. Mode I fracture toughness, upon annealing, increased

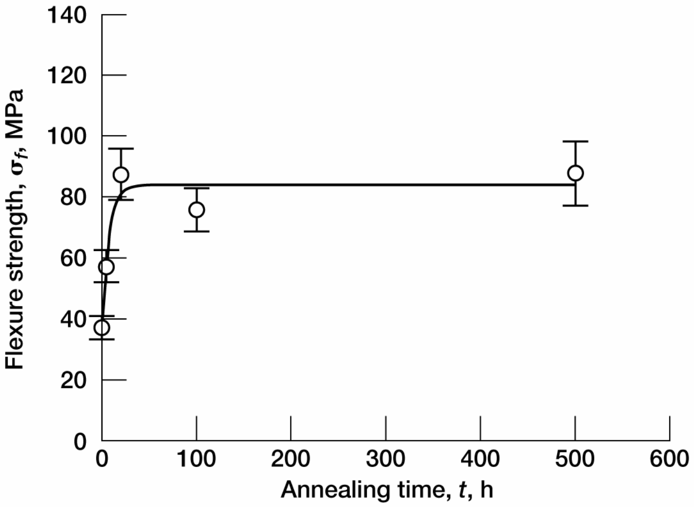

Figure 6.—Flexure strength as function of annealing time for plasma-sprayed ZrO_2-8 wt% Y_2O_3 thermal barrier coatings annealed at 1316 °C in air. Error bars indicate ±1.0 standard deviation.

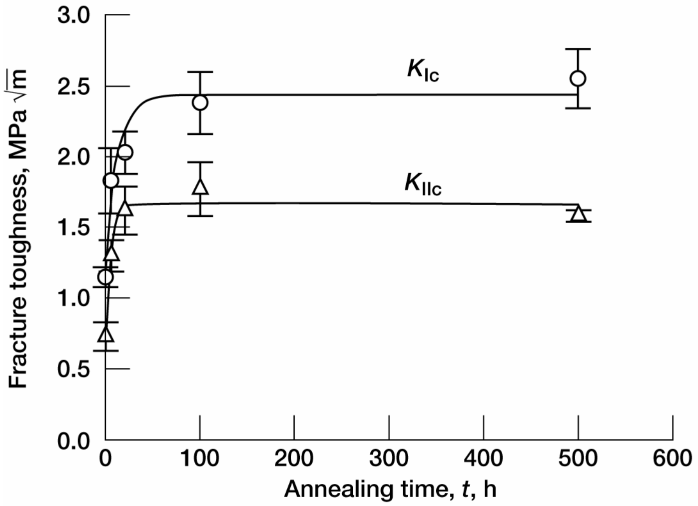

Figure 7.—Fracture toughnesses K_{Ic} and K_{IIc} as function of annealing time for plasma-sprayed ZrO_2-8 wt% Y_2O_3 thermal barrier coatings annealed at 1316 °C in air. Fracture toughness determined by single-edge-V-notched-beam (SEVNB) method. Error bars indicate ±1.0 standard deviation.

significantly up to t = 100 h and then reached a plateau thereafter with $K_{Ic} = 2.6 \pm 0.2$ MPa$\sqrt{m}$ at t = 500 h, which is about a 120-percent increase from t = 0. It is noted that unlike strength, fracture toughness of TBCs at the plateau region was considerably greater than that (K_{Ic}=1.7 MPa$\sqrt{m}$) of hot-pressed 10 mol% YSZ (ref. 27), presumably due to the increased crack resistance of TBCs as a result of a change to a sintered, densified material body. Similar to the case in mode I, fracture toughness in mode II increased rapidly within 20 h, and then reached a plateau at $t \geq 100$ h with an approximate 140-percent increase at t = 100 h. This increase in K_{IIc} compares well with that (120 percent) in K_{Ic} as well as that (130 percent) in strength.

The ratio $K_{\mathrm{IIc}}/K_{\mathrm{Ic}}$ for a given annealing time did not vary significantly, ranging from 0.63 to 0.80 with a resulting average of $K_{\mathrm{IIc}}/K_{\mathrm{Ic}} = 0.70 \pm 0.08$ for t = 0 to 500 h. It has been reported that for some dense ceramics K_{IIc} was greater than K_{Ic}, attributed to the frictional interaction between the two crack planes (ref. 28). However, the previous studies on advanced ceramics including silicon nitrides, alumina, and zirconia (refs. 29 and 30) showed a different result that K_{IIc} was almost identical to K_{Ic}, indicative of insignificant frictional effects on K_{IIc}, regardless of either coarse-grained or fine-grained structures. The coating material yielded lower K_{IIc} than K_{Ic} values in both as-sprayed and annealed conditions. It is believed that the coating material would fracture easier in shear (mode II) than in cleavage (mode I), because of its unique open, microcracked splat (platelet) structure, thereby resulting in low K_{IIc}.

The critical crack size at failure was estimated as a function of annealing time using the already determined values of respective flexure strength and fracture toughness, based on an assumption of half-penny-shaped crack configuration. The stress intensity factor related to such a crack configuration in an infinite body[1] is expressed as follows (ref. 22):

$$K_{\mathrm{I}} = Y\sigma_f \sqrt{\pi c_f} \tag{6}$$

where Y is the crack geometry factor ($Y = 2/\pi$) and c_f is the critical crack size. The critical crack sizes[2] based on equation (6) were estimated to be 760, 800, 420, 780, and 660 μm, respectively, for t = 0, 5, 20, 100, and 500 h. Except for the value at t = 20 h, the estimated crack sizes were not significantly different. Use of more test specimens in strength testing, of course, can yield more statistically reliable crack-size data. The current crack-size data, nonetheless, provides the insight that *strength-controlling* cracks or flaws in as-sprayed TBCs would remain reasonably unchanged in size, regardless of the sintering duration. This, from a fracture mechanics point of view, leads to the conclusion that fracture toughness is the only variable to affect the magnitude of strength of either the as-sprayed or annealed body of the current TBC system. This conclusion might be contrary to the notion that sintering would result in a decrease in crack and flaw size via healing or grain growth, thus leading to an increase in strength. Although micro- or macrocracks and pores might be healed or filled via the annealing-sintering process, which gives rise to an increase in fracture toughness, major *strength-controlling* cracks or flaws having significant crack (or flaw) openings would be little affected in their overall physical sizes upon annealing. This suggests a necessity of simultaneous evaluation of both strength and fracture toughness of TBCs as sprayed or annealed; otherwise, a misleading interpretation could be attained regarding crack or flaw size if only one property, say strength, is used. This is particularly important in TBCs for which fractography, used to determine crack and flaw sizes as well as their configurations, is extremely difficult.

---

[1] The stress intensity factor (SIF) for a half-penny-shaped crack in a finite plate under flexure is expressed (ref. 22) as

$$K_{\mathrm{I}} = H\sigma\sqrt{\pi\frac{c}{Q}}\; F\left(\frac{c}{W}, \frac{c}{b}, \phi\right)$$

where H, Q, and F are crack-geometry and specimen-dimension-dependent functions, σ is remote outer-fiber flexure stress, c is crack size, and ϕ is an angle of a particular point in crack front measured from specimen surface. The maximum SIF occurs at $\phi = 0$; i.e., at the specimen surface. It can be also found that the maximum SIF varies by only a few percents (about 6 percent) even though c/W varies between 0.2 and 0.5. Therefore, a closed form, infinite body solution without considering the complexity associated with crack and specimen size corrections in functions H, Q, and F can be used, which leads to equation (6).

[2] The exact configuration of critical cracks whether they were either in single cracks or in multiple cracks connected to each other was not certain, due to difficulty in fractography. Hence, the term "critical crack" can include a meaning of "apparent" or "resultant" critical cracks.

Elastic Modulus

The stress-strain curves of TBCs in compression determined for different annealing times by strain gaging are shown in figure 8. The as-sprayed cylindrical rod test specimen exhibited unique nonlinearity in both loading and unloading curves with significant hysteresis, primarily due to internal friction from the loosely connected open structure (refs. 12, 13, 31, and 32). This type of nonlinear behavior also has been observed in sandstone (ref. 15) that exhibited an open microstructure similar to as-sprayed TBCs. Furthermore, the behavior is also analogous to the phenomenon observed in stress-strain curves of dense brittle materials, involved with frictional constraint in four-point flexure testing when rollers are fixed (i.e., not free to move) (ref. 31). Despite its nonlinearity, the as-sprayed test specimen revealed almost completely elastic behavior with little plastic deformation. This nonlinear elastic behavior was found to be independent of the loading rate, number of cycles, and type of loading configurations (flexure, tension, or compression) (refs. 12, 13, and 15). As annealing time increased, both nonlinearity and hysteresis decreased. At $t \geq 20$ h, the annealed test specimens exhibited reasonably well-developed linear constitutive relations with little hysteresis.

Elastic modulus E, determined from the slope of each stress-strain curve in figure 8, was plotted as a function of annealing time in figure 9. The elastic modulus of each test specimen annealed at $t = 0$ or 5 h was determined from the slope of a straight line drawn from zero to peak load, although a single value of elastic modulus can be never defined particularly in as-sprayed TBCs. Elastic modulus, as seen in the figure, increased quickly from $E = 25$ to 55 GPa within a short period of time $t = 20$ h and reached a plateau at $t \geq 100$ h with $E = 75$ GPa. Hence, a significant increase in elastic modulus by about 200 percent resulted from annealing at $t \geq 100$ h, much greater than the 120- to 130-percent increase in strength and fracture toughness. The elastic modulus in the plateau, however, was considerably lower than that ($E = 219$ GPa) of dense 10 mol% YSZ (ref. 27), indicating that the annealed TBC body was still of an open, loose structure, compared to the dense ceramic, even after a long sintering of $t = 500$ h.

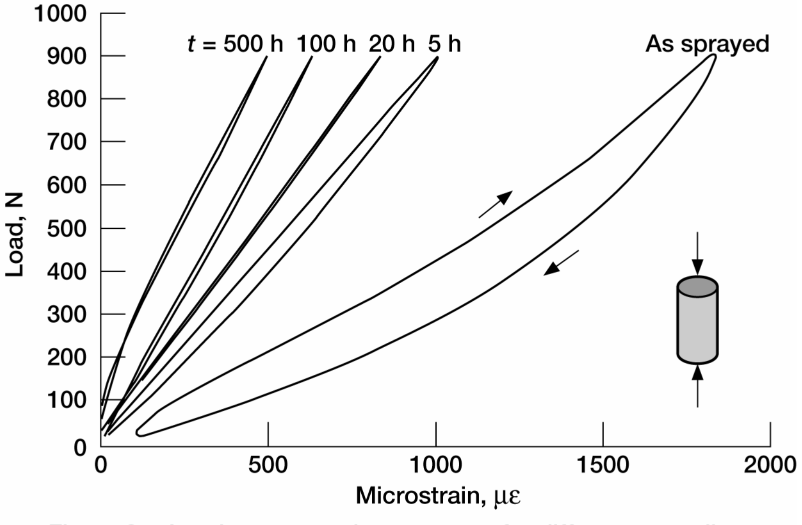

Figure 8.—Load versus strain responses for different annealing times t of plasma-sprayed ZrO_2-8 wt% Y_2O_3 thermal barrier coatings annealed at 1316 °C in air, determined in compression with cylindrical rod specimens by strain gaging.

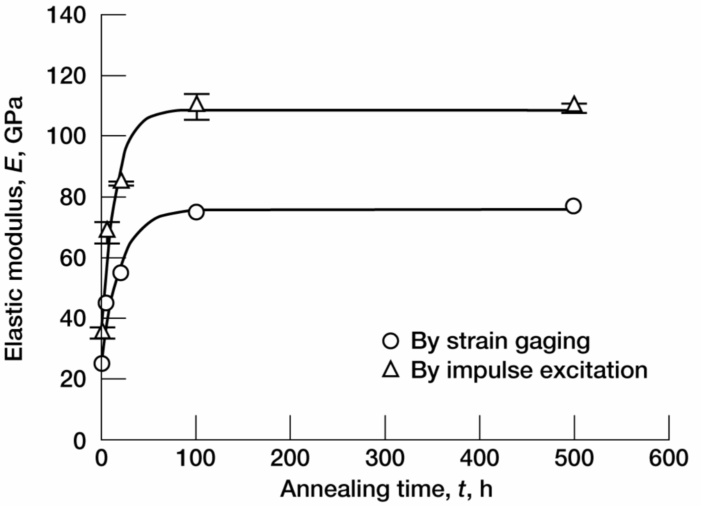

Figure 9.—Elastic modulus as function of annealing time for plasma-sprayed ZrO_2-8 wt% Y_2O_3 thermal barrier coatings annealed at 1316 °C in air. Elastic modulus determined by both strain gaging in compression and impulse excitation in flexure. Error bars indicate ±1.0 standard deviation.

Figure 9 also includes the elastic modulus determined with flexure bars by the impulse excitation method (ref. 24). Fundamental resonant frequency was invariably defined either in as-sprayed or in annealed test specimens. The general trend of elastic modulus with respect to annealing time was almost identical to that determined by strain gaging. However, the magnitude of elastic modulus for a given time was consistently greater by 64 to 68 percent in the excitation method than in the strain gaging, in contrast with general observations that most dense, homogeneous materials exhibit negligible or almost no difference in elastic modulus between the two methods. The reason for the elastic-modulus difference in TBCs between the two methods is not clear yet. Difference in the mode of deformation—large strain in uniaxial compression (strain gaging) versus small strain in uniaxial vibratory flexure (excitation method)—incorporated with the open, loose splat structure of TBCs might be a plausible reason.

Poisson’s Response

Typical examples of both longitudinal and lateral strain components of cylindrical rod specimens in compression are presented in figure 10, for as-sprayed (t = 0 h) and annealed (t = 500 h) test specimens. For the as-sprayed specimen, the lateral strain (ε_2) was not as responsive as the longitudinal strain (ε_1), so that a single, fixed value of Poisson’s ratio ($\nu = |\varepsilon_2/\varepsilon_1|$) was barely able to be defined. At the peak load, for example, the value of $|\varepsilon_2/\varepsilon_1|$ was around 0.03. By contrast, for the annealed specimen, both the lateral and longitudinal strains responded well to compression loading, resulting in a reasonably well-defined Poisson’s ratio of about $\nu = 0.2$. This result again indicates that a more open, loosely connected structure was typified in the as-sprayed condition, whereas a less open and somewhat tightly connected or densified structure was characterized in the annealed condition.

Density

Figure 11 shows the change in density as a function of annealing time. Density was determined here based on the bulk mass-volume approach. The overall trend in density was similar to that in strength,

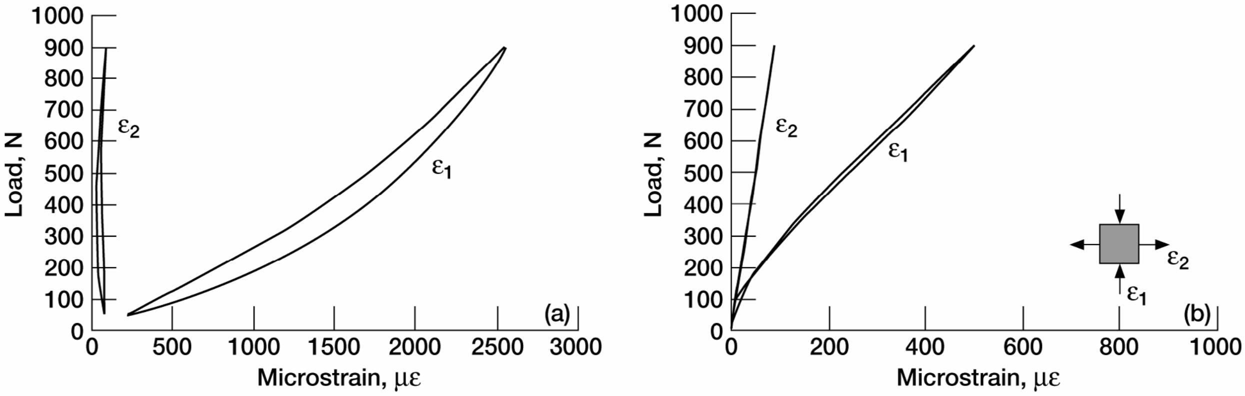

Figure 10.—Load versus longitudinal (ε_1) and lateral (ε_2) strains in compression for plasma-sprayed ZrO_2-8 wt% Y_2O_3 thermal barrier coatings annealed at 1316 °C in air for different times *t*. (a) *t* = 0 h. (b) *t* = 500 h.

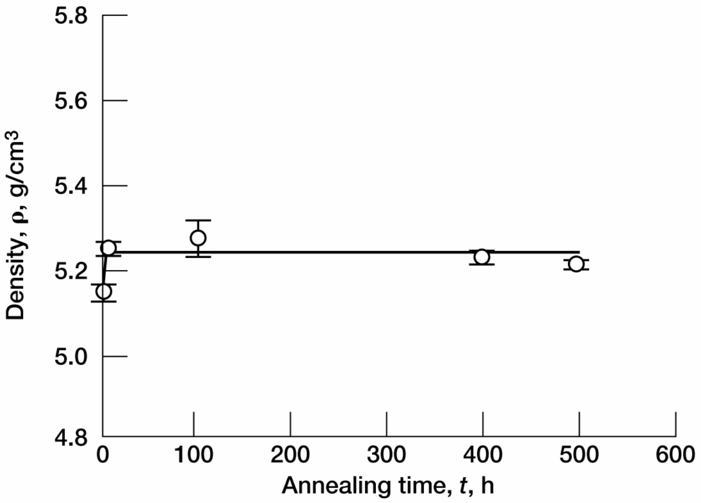

Figure 11.—Density as function of annealing time for plasma-sprayed ZrO_2-8 wt% Y_2O_3 thermal barrier coatings annealed at 1316 °C in air. Error bars indicate ±1.0 standard deviation.

fracture toughness, and elastic modulus, except for the degree in increase and the time to reach a plateau. The density increased from the as-sprayed value of 5.15±0.02 g/cm^3 by 2.0, 2.5, 1.6, and 1.3 percent, respectively, at *t* = 5, 100, 400, and 500 h. This increase in density was observed as a result of dimensional change (contraction) of flexure test specimens upon annealing, while their respective masses remained unchanged, independent of time. Note that two test specimens (with a full length) were used progressively from *t* = 0 to *t* = 500 h to determine their elastic modulus and density as a function of time, as mentioned in the "Experimental Procedures" section.

The plateau in density was formed at an earlier time of *t* = 5 h, compared with that formed at *t* = 20 or 100 h in strength, fracture toughness, or elastic modulus. Note that the density of dense 10 mol% YSZ is 5.839 g/cm^3 (ref. 27). The maximum density of TBCs achieved by annealing at 1316 °C was about 90 percent of the density of 10 mol% YSZ with a resulting porosity of about 10 percent, whereas the density of as-sprayed TBCs was about 88 percent of the 10 mol% YSZ counterpart with a resulting porosity of 12 percent, in agreement with a mercury porosity method from a previous study (ref. 33). As a consequence, a small increase (2 percent) in density due to annealing-sintering resulted in a significant change in mechanical properties such as strength, fracture toughness, and elastic modulus. However, the degree of sensitivity in mechanical properties with respect to density variation was significantly greater in dense ceramics (e.g., silicon nitrides) (ref. 34) than TBCs. It might be argued that annealing for a long time (e.g., 500 h) at 1316 °C in air might have changed the weight of test specimens due to oxidation, adding an inherent error in the density measurement; however, the weight change by oxidation was found to be negligible with only a 0.03 percent decrease from the as-sprayed counterpart.

Hardness

Because of the presence of microcracks and porosity, Vickers microhardness impressions in TBCs were not as easily and clearly defined as those in dense ceramics. Surface cracks and pores obscured the impression measurements, giving increased uncertainty. Although hardness impressions seemed a little better defined in their configuration for annealed TBCs, the overall uncertainty in impression measurements was about the same as that for the as-sprayed specimens. The overall results of Vickers hardness measurements as a function of annealing time, determined at indentation loads P_i of 9.8 and 19.6 N, are depicted in figure 12. As in some of the mechanical properties and density, hardness increased quickly at $t = 5$ h, seemingly reaching a plateau at $t \leq 100$ h. The hardness values at 9.8 N were about 25 percent greater than those at 19.6 N, attributed to the localized densification (plastic deformation) that occurs upon indentation: less localized densification would occur with a lower P_i.

For a given surface, the variation in microhardness H with respect to different locations appeared to be insignificant: $H = 6.46 \pm 1.18$, 6.52 ± 1.17, and 6.24 ± 1.25 GPa, respectively, in rows 1, 2, and 3, as designated in figure 13. The average with a total of 30 indents was $H = 6.43 \pm 1.21$ GPa. Table II presents the microhardness values at these locations for a 100-h annealed specimen at a P_i of 9.8 N. Values from row 1 measurements were used in figure 12.

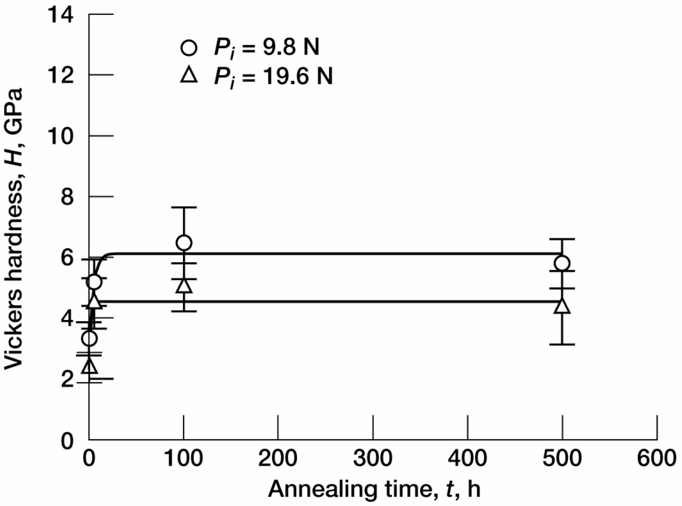

Figure 12.—Vickers hardness as function of annealing time for plasma-sprayed ZrO_2-8 wt% Y_2O_3 thermal barrier coatings annealed at 1316 °C in air, determined at two different indentation loads P_i of 9.8 and 19.6 N. Measurements taken at row 1 location (from fig. 13). Error bars indicate ±1.0 standard deviation.

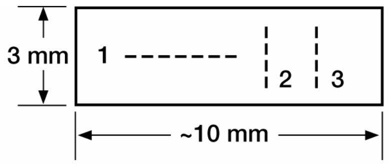

Figure 13.—Surface of ZrO_2-8 wt% Y_2O_3 thermal barrier coating specimen (normal to plasma-spraying direction), showing location of rows along which indents were made for Vickers hardness measurements.

TABLE II.—VICKERS HARDNESS OF ZrO_2-8 WT% Y_2O_3 THERMAL BARRIER COATINGS

[Sintered at 1316 °C in air, 100 h; indent load, 9.8 N at top surface.]

Location of rows[a]	Number of indents	Vickers microhardness,[b] *H*, GPa
Row 1	20	6.46(1.18)
Row 2	5	6.52(1.17)
Row 3	5	6.24(1.25)
Grand total	30	6.43(1.21)

[a] Rows depicted in fig. 13.

[b] Numbers in parentheses represent ±1.0 standard deviation.

Unlike dense ceramics, TBCs exhibited significant scatter in microhardness; the coefficient of variation ranged from 12 to 20 percent, almost independent of annealing time or indentation load. This consistent but significant scatter was primarily due to the loosely connected open structure of TBCs (about 10 to 12 percent porosity, see the "Density" section), making the material microscopically inhomogeneous in response to microindentation. In addition, pore or flaws in some cases were comparable to the impression sizes of 50 to 100 μm, which made the impression size measurements obscure, thereby increasing uncertainty in hardness measurements. For dense 10 mol% YSZ, microhardness is around $H = 14$ GPa with insignificant scatter, having a coefficient of variation of 4 percent (ref. 29). Typical Weibull hardness distributions of the 100-h annealed TBCs from measurements at row 1 (see fig. 13) with both 9.8 and 19.6 N are presented in figure 14. A relatively low Weibull modulus (slope) of around 7 to 8 was observed at both loads and was thus characterized as a unique response of plasma-sprayed TBCs to elastic-plastic microindentation deformation. For dense ceramics such as 10 mol% YSZ, the Weibull modulus in microhardness distribution is around 30.

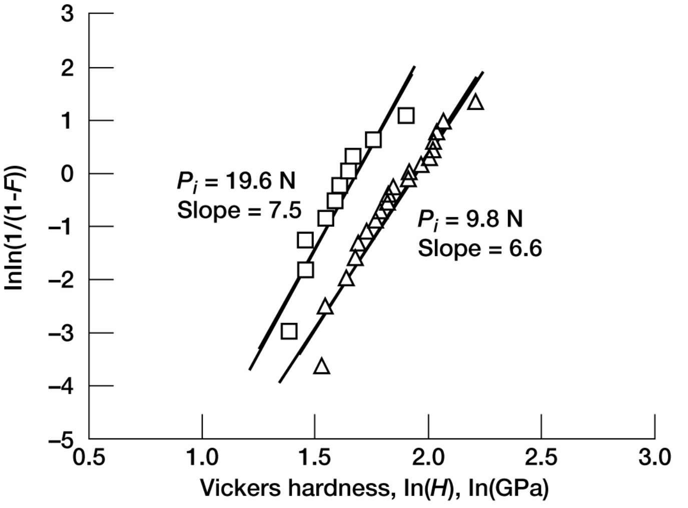

Figure 14.—Typical Weibull hardness distributions of plasma-sprayed ZrO_2-8 wt% Y_2O_3 thermal barrier coatings annealed for 100 h at 1316 °C in air, determined by Vickers indenter at indentation loads P_i of 9.8 and 19.6 N at row 1 location (from fig. 13).

Surface Structure and Fractography

Scanning electron microscopy (SEM) of polished surfaces of TBCs did provide some information regarding microcrack and/or pore healing as a result of sintering. Pores and microcracks were similarly present in either as-sprayed or annealed specimens, although the 100- and 500-h-annealed specimens showed a little decreased severity in pores and microcracks, as displayed in figure 15. The surfaces of the annealed specimens were much smoother than the as-sprayed counterparts. A change in color from dull yellow to a somewhat shiny white-yellow was also noted for the specimens annealed particularly at longer times.

Figure 16 shows fracture surfaces with respect to annealing time for specimens tested in mode I fracture toughness testing. Large amounts of microcracks and pores were typically seen in splats and at splat boundaries on the as-sprayed specimen. For specimens annealed at *t* = 20 and 100 h, both initiation and development of grain growth due to the sintering effect were evident with grain growth being more dominant for the specimen annealed for a longer time of *t* = 100 h. Big pores and major cracks particularly located at the splat boundaries with noticeable crack opening displacement (COD) did not change significantly in their sizes upon annealing; however, small pores, gaps, or microcracks both in and between splats were diminished by the increase in contact areas between the splats and between splat

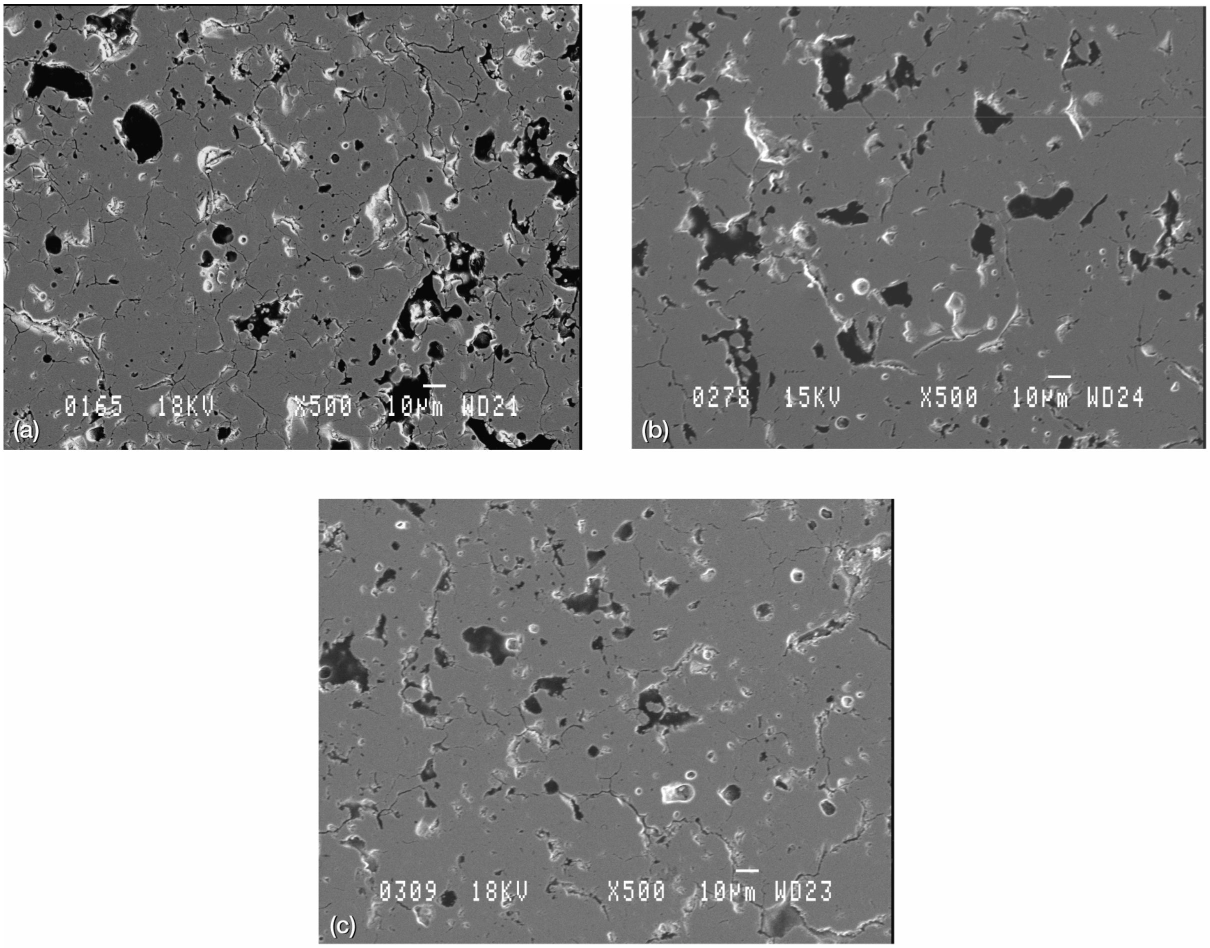

Figure 15.—Polished surfaces of plasma-sprayed ZrO_2-8 wt% Y_2O_3 thermal barrier coatings by SEM, annealed at 1316 °C in air at different times *t*. (a) *t* = 0 h (as sprayed). (b) *t* = 100 h. (c) *t* = 500 h.

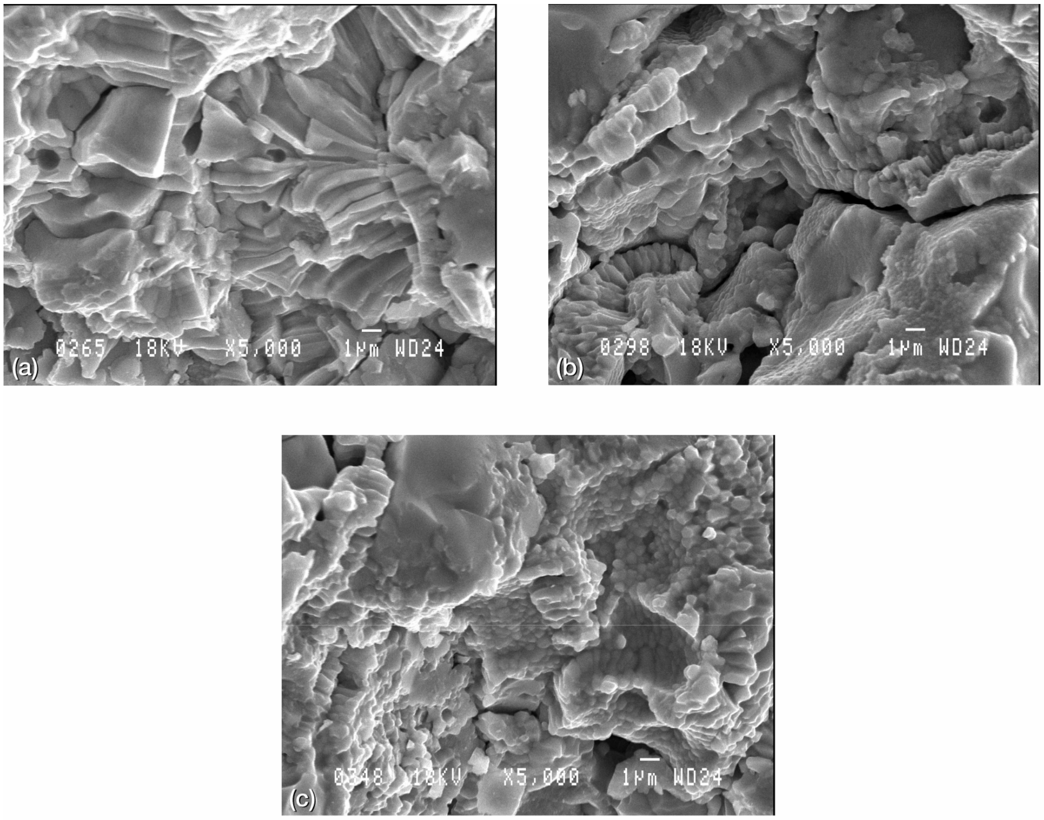

Figure 16.—Fracture surfaces of mode I fracture toughness specimens of plasma-sprayed ZrO_2-8 wt% Y_2O_3 thermal barrier coatings annealed at 1316 °C in air at different times, t. (a) t = 0 h (as sprayed). (b) t = 20 h. (c) t = 100 h.

particles, as noted previously (refs. 4, 5, 7, and 8). Although microcracks *inside* bulk TBCs would be "healed" (filled out) upon annealing by the process of grain growth, this must be differentiated from the conventional crack healing process of many advanced dense ceramics, in which crack healing occurs because of oxidation—not grain growth—by filling *surface* microcracks with oxidation products.

It has been understood that sintering in plasma-sprayed TBCs is governed by bridging between the splat particles at sites in intimate physical contact. This bridging leads to chemical bonding via grain growth between the splat particles and within the splats, diminishing small pores and microcracks. However, large microcracks with significant COD and big pores in splats and at splat boundaries, which are not in close physical contact, remain relatively immune to sintering (refs. 4, 7, and 8). This is also inferred from the fact the estimated critical crack sizes at failure remained relatively unchanged, regardless of annealing time (see "Fracture Toughness" results section).

Thermal Conductivity

Although sintering, from a mechanical-property viewpoint, gives favorable results such as increased strength and fracture toughness, it also gives an adverse effect stemming from a change in microstructure from open and loosely connected to more tightly closed, resulting in a more densified and stiffer network of the TBC body. This microstructural change is expected to have a considerable influence on the inherently unique function of plasma-sprayed TBCs by increasing thermal conductivity (refs. 4, 6, and 35) and reducing strain tolerance (expansivity). An example of a change in thermal conductivity as a function of time (from ref. 6) is shown in figure 17, in which testing was conducted in air under high heat flux

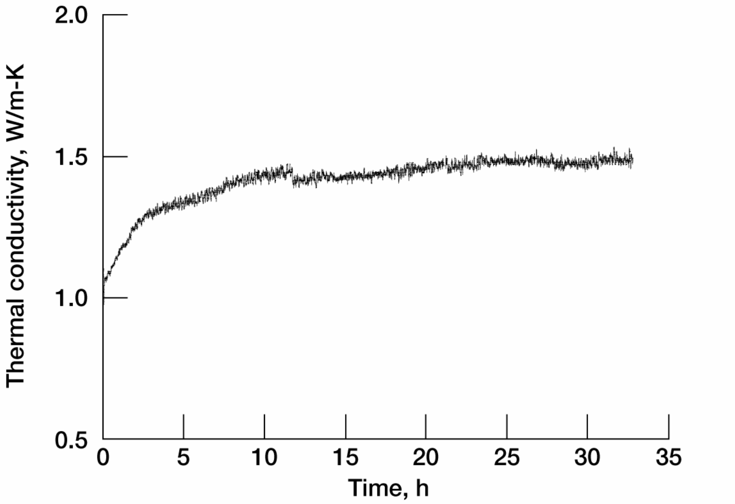

Figure 17.—Thermal conductivity as function of time for plasma-sprayed ZrO_2-8 wt% Y_2O_3 thermal barrier coatings at surface temperature of 1320 °C in air under high-heat-flux conditions by laser (ref. 6).

conditions by a laser, maintaining a surface temperature of 1320 °C. A similarity in behavior between mechanical properties and thermal conductivity is manifest from the figure such that a significant thermal conductivity increase occurred at $t \leq 5$ to 10 h, followed by a plateau thereafter. Resistance to sintering, while maintaining a low thermal conductivity, particularly at higher temperatures, is of prime importance in performance and life of a TBC system. Extensive efforts towards development of more sinter-resistant and higher temperature TBCs are under way (refs. 36 to 38).

Phase Stability

The plasma-sprayed, partially stabilized ZrO_2-8 wt% Y_2O_3 coatings can degrade during high-temperature exposure because of the nontransformable tetragonal t′ phase separation into a low-yttria, transformable tetragonal phase and a high-yttria cubic phase. The low-yttria tetragonal phase can transform to the lower temperature monoclinic phase upon cooling or thermal cycling. The monoclinic phase transformation is accompanied by significant volume expansion (3 to 5 vol%) and thus can result in severe coating cracking and significant coating mechanical property degradation.

Figure 18 shows the amount of the monoclinic phase as a function of annealing time at 1316 °C. It can be seen that the amount of monoclinic phase showed a considerable increase with increasing time under the furnace heating and cooling condition, as observed for the other coating properties. The monoclinic phase amount remained at 2 to 3 mol% in the first 5 h, but increased rapidly to 7 to 8 mol% after 100 h. The monoclinic phase amount seemed to saturate and reach a final value around 10 to 11 mol% after 500 h. The slow furnace cooling rate in the present study seemed to transform more monoclinic phase amount for the plasma-sprayed coatings than some of the more rapid cooling cases examined previously (ref. 39 and D. Zhu and R. A. Miller, 2001, National Aeronautics and Space Administration, Glenn Research Center, Cleveland, OH, unpublished work).

Although a general increasing trend is observed for the amount of monoclinic phase formation with annealing, the monoclinic phase increase showed a slower response with respect to the annealing time as compared to the mechanical properties, density, and thermal conductivity. This is because the monoclinic phase formation is mainly associated with the diffusion-related partitioning of some of the metastable

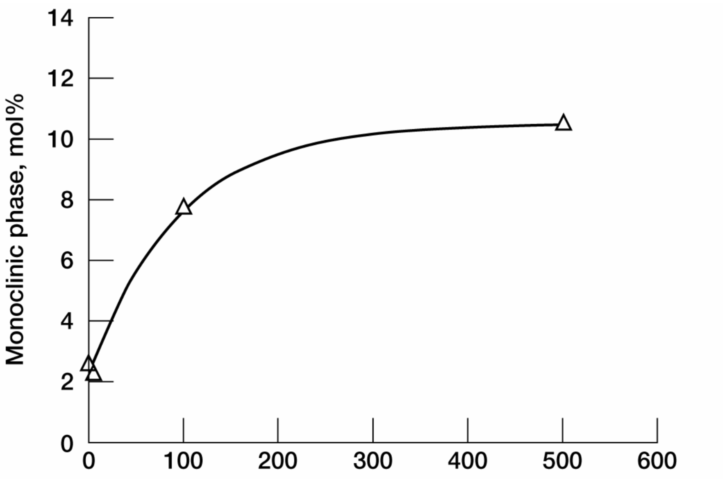

Figure 18.—Percent of monoclinic phase as function of annealing time of plasma-sprayed ZrO_2-8 wt% Y_2O_3 thermal barrier coatings annealed at 1316 °C in air.

tetragonal t′ phase and the subsequent transformation into the monoclinic phase. This process is not closely related to the density increase of the material.

Modeling

A model to quantify the time-dependent coating property behavior at 1316 °C is proposed by normalizing the property-value increases at a given time and then fitting them into an exponential growth formulation as follows:

$$\frac{q_c - q_c^0}{q_c^{\text{inf}} - q_c^0} = C \cdot \exp\left[1 - \exp\left(-\frac{t}{\gamma}\right)\right] \tag{7}$$

where q_c is the value of any property at a given annealing time t, q_c^0 and q_c^{inf} are the corresponding values at the initial time and at an infinite long time, respectively, γ is the relaxation time, and C is a constant related to temperature. It should be mentioned that in all cases $C = 1$ because q_c^{inf} is taken as the final value of the property at the only test temperature of 1316 °C (instead of using the material intrinsic value). This model has been used to describe elastic modulus evolution of TBCs under a high heat flux condition by a laser (ref. 6).

The results based on the model incorporated with experimental data are shown in figure 19. Figure 19(a) shows that most of the properties, except for the monoclinic phase content, reached their final values within a relatively short time and are characterized by a relatively short relaxation time γ. Figure 19(b) shows that the relaxation time for various properties, determined from a functional fit analysis, ranged narrowly from 10 000 to 60 000 s (2.7 to 17 h). The relatively short relaxation time for these properties suggests that they are strongly related to the coating microcracks and splat boundaries, which tend to be sintered away quickly because of the fast surface and boundary diffusion. In a comparison of the investigated properties, a property with a shorter relaxation time may imply a stronger dependence on the coating microcracks, whereas one with a longer relaxation time may suggest a stronger dependence on

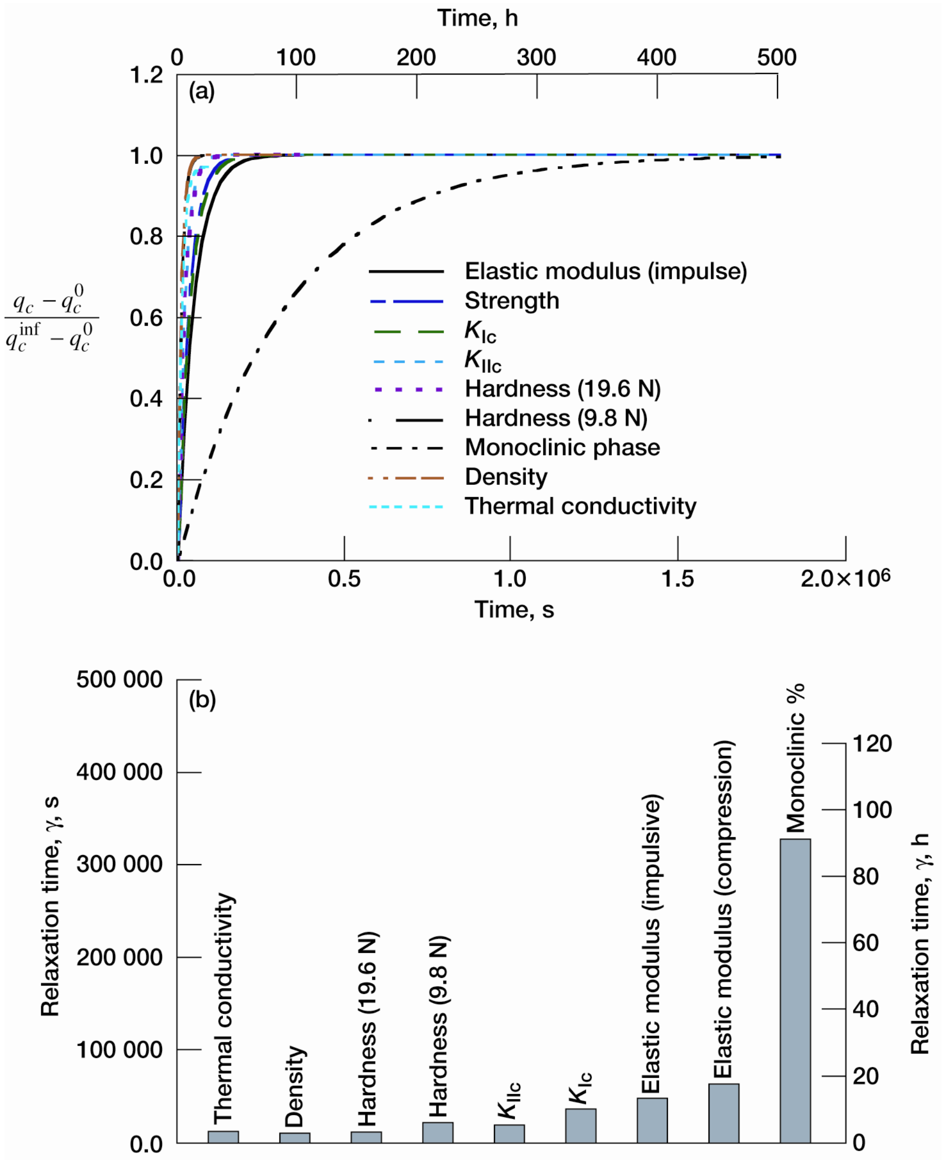

Figure 19.—Results of application of model (eq. (7)) to various property values determined in this study. (a) Resulting plots of eq. (7). (b) Summary of relaxation times γ determined for various properties.

the large-sized microcracks or pores. For example, the coating thermal conductivity is likely more sensitive to the microcracks than the elastic modulus as determined from its shorter relaxation time. The t′ phase partitioning (later resulting in the monoclinic phase formation) is related to the volume diffusion of cations and anions. Therefore, the phase transformation will have a much longer relaxation time than other properties that are more sensitive to the surface-diffusion-related microcrack sintering.

Although the model was not based on a rigorous physical and theoretical foundation, it nevertheless allows one to quantify and assess the phenomenological effect of sintering on various property quantities in a convenient and expedient manner. Furthermore, the model could be used to construct a universal sintering map to include more variables such as different temperatures and different ceramic coating materials as well.

Directionality of As-Sprayed TBCs

TBCs were fabricated via plasma-spray process so that anisotropy might be expected because of the prevailing open, splat structure, preferably aligned with respect to spraying direction. The effect of such anisotropy, as mentioned in Experimental Procedure, was determined for as-sprayed TBCs through mode I fracture toughness, Knoop microhardness, and elastic modulus testing. The results are summarized in table III. The values of fracture toughness were found to be $K_{\mathrm{Ic}} = 1.15 \pm 0.07$, 1.04 ± 0.11, and 1.04 ± 0.05 MPa $\sqrt{\mathrm{m}}$, respectively, in directions 1, 2, and 3 (see fig. 5). Contrary to the expectation, fracture toughness yielded an almost consistent value with only a 10-percent variation in three directions, showing an insignificant response to directionality. The expected weakest direction (interlaminar, direction 3) yielded a value of fracture toughness identical to the presumably strongest counterpart (direction 2).

The results of Knoop microhardness as a function of material axis are also shown in table III. A particular interest is in the side surface: The value ($H = 3.25$ GPa) of microhardness parallel to the layers (at 0°) was not significantly different from that (3.19 GPa) perpendicular to the layers (at 90°). Typical examples of Knoop indents made in the side surface at both 0° and 90° angles are shown in figure 20. Knoop microhardness also exhibited little difference between 0° and 90° directions in the top surface, resulting in similar values to those in the side surface. This indicates that as-sprayed TBCs exhibited macroscopically “homogeneous” response to microhardness deformation, as was seen with the results of fracture toughness. Little discrepancy in Vickers microhardness was observed between the side and the top surfaces (see table III), too. It is also noted that difference between Knoop and Vickers microhardness was negligible.

The elastic modulus additionally determined in direction 2 by the impulse excitation technique was found to be $E = 39 \pm 2$ GPa, which compares well with $E = 36 \pm 2$ found in direction 1. Note that the same three specimens were used in both directions 1 and 2. An 8-percent variation in elastic modulus between the two directions is again indicative of an insignificant directionality effect of the as-sprayed TBCs on elastic modulus.

TABLE III.—MODE I FRACTURE TOUGHNESS, MICROHARDNESS, AND ELASTIC MODULUS WITH RESPECT TO MATERIAL DIRECTION OR SURFACE FOR AS-SPRAYED ZrO_2-8 WT% Y_2O_3 THERMAL BARRIER COATINGS AT AMBIENT TEMPERATURE

Type of testing	Direction or surface[a]	Method[b]	Number of tests	Value[c,d]
Fracture toughness	1	SEVNB	5	$K_{\mathrm{Ic}} = 1.15(0.07)$ MPa $\sqrt{\mathrm{m}}$
	2	SEVNB	4	$K_{\mathrm{Ic}} = 1.04(0.11)$ MPa $\sqrt{\mathrm{m}}$
	3	DCB	3	$K_{\mathrm{Ic}} = 1.04(0.05)$ MPa $\sqrt{\mathrm{m}}$
				$K_{\mathrm{Ic}} = 1.09(0.07)$ MPa $\sqrt{\mathrm{m}}$
Microhardness	0°; side surface	Knoop	5	$H = 3.25(0.32)$ GPa
	90°; side surface	Knoop	5	$H = 3.19(0.86)$ GPa
	0°; top surface	Knoop	5	$H = 3.31(0.55)$ GPa
	90°; top surface	Knoop	5	$H = 3.68(1.27)$ GPa
				$H = 3.36(0.45)$ GPa
	Top surface	Vickers	5	$H = 3.13(1.16)$ GPa
	Side surface	Vickers	5	$H = 3.23(0.84)$ GPa
				$H = 3.18(0.92)$ GPa
Elastic modulus	1	Impulse excitation	3	$E = 35.6(2.0)$ GPa
	2	Impulse excitation	3	$E = 38.8(2.2)$ GPa

[a] See figure 5 for orientations and material directions.

[b] SEVNB is single-edge-v-notched beam; DCB, double cantilever beam.

[c] Numbers in parentheses represent ±1.0 standard deviation.

[d] Numbers in bold represent average values.

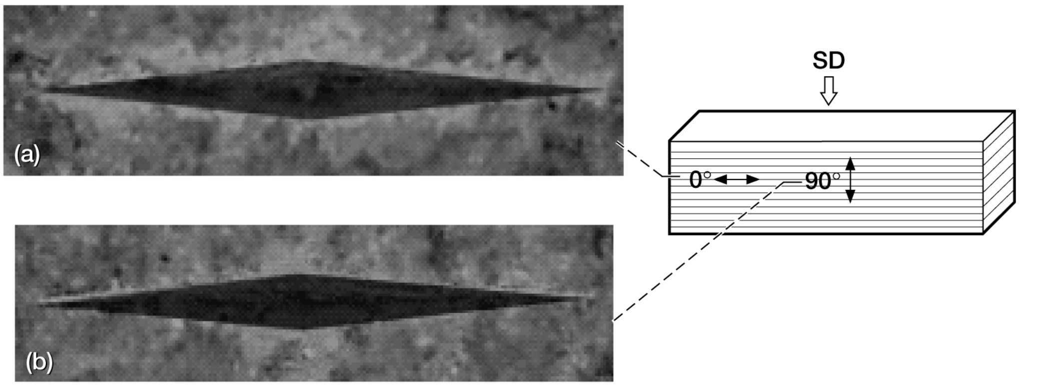

Figure 20.—Typical Knoop indents made in side surface of as-sprayed ZrO_2-8 wt% Y_2O_3 thermal barrier coatings at ambient temperature at different directions to the lamellar-like layers. (a) Parallel (0°). (b) Normal (90°).

Fracture toughness, microhardness and elastic modulus, normalized with respect to corresponding respective reference values, are summarized in figure 21. A conclusion regarding the directionality effect can be readily made from the summary: Despite their unique microstructure possessing interlaminar-like layers and oriented splats, the as-sprayed TBCs used in this work can be categorized as a "homogeneous" material from a perspective of *macroscopic* continuum mechanics.

Properties Summary

All properties determined in this work as a function of annealing time are summarized in table IV.

Summary of Results

Mechanical and physical properties of free-standing plasma-sprayed ZrO_2-8 wt% Y_2O_3 thermal barrier coatings (TBCs) annealed at 1316 °C in air were determined at ambient temperature as a function of annealing time ranging from 0 to 500 h. The mechanical and physical properties thus determined included flexure strength, modes I and II fracture toughness, elastic modulus, Poisson's response, density, microhardness, surface structure and fractography, and phase stability. Except for phase stability, all properties increased significantly in 5 to 100 h and then reached a plateau above 100 h; the percentage of monoclinic phase increased monotonically without forming a plateau. Annealing, which provided a sintering effect, resulted in microcrack and pore healing, grain growth, and densification so that a loosely connected, open structure was changed into more closely connected, densified structure. However, an inevitable adverse effect also occurred such that the relatively low thermal conductivity and good expansivity—which make the TBCs unique in thermal barrier applications—were degraded upon annealing because of the densified network of the TBC body. The proposed model quantified well all related property variables as a function of annealing time in a simple normalized fashion. Directionality of as-sprayed TBCs was found to be macroscopically negligible through the determinations of fracture toughness, microhardness, and elastic modulus with respect to material direction.

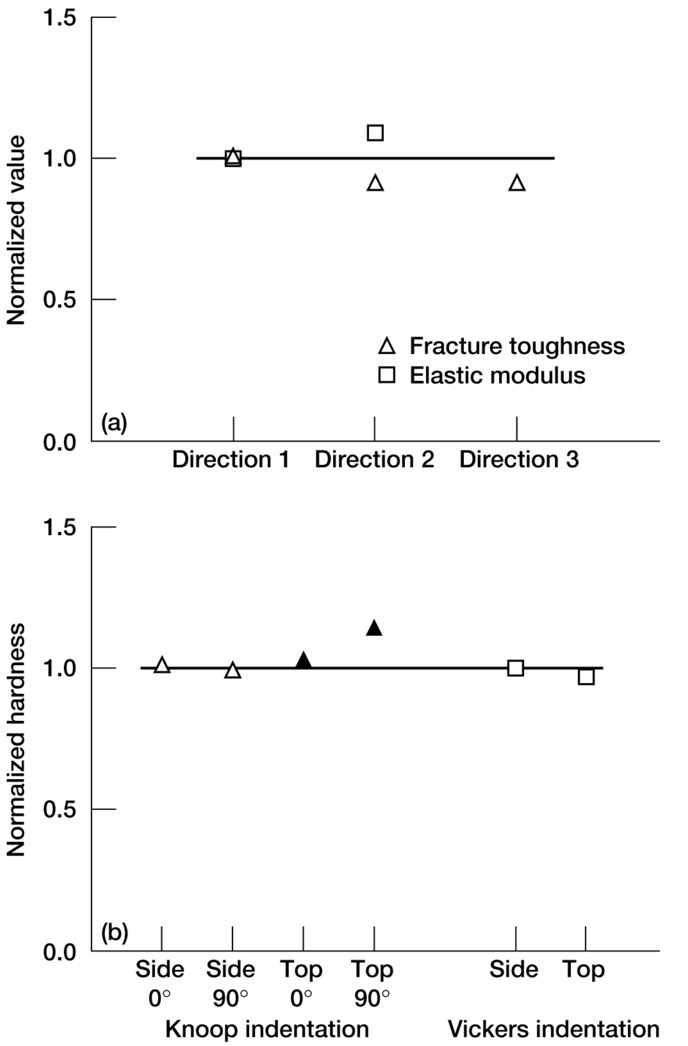

Figure 21.—Normalized material properties with respect to material direction for as-sprayed ZrO_2-8 wt% Y_2O_3 thermal barrier coatings. For definitions of direction and orientation surfaces, see figure 5. (a) Fracture toughness and elastic modulus. Normalized with respect to values determined in direction 1. (b) Microhardness determined in both top and side surfaces. Knoop hardness determined at 0° and 90° angles for indentation with a load of 9.8 N, normalized with respect to value of side at 0°. Vickers hardness determined in both side and top surfaces with a load of 9.8 N, normalized with respect to value from side surface.

TABLE IV.—PROPERTIES DETERMINED AS FUNCTION OF ANNEALING TIME FOR PLASMA-SPRAYED ZrO_2-8 WT% Y_2O_3 THERMAL BARRIER COATINGS
[Annealed at 1316 °C in air.]

Sintering time, t, h	Flexure strength,[a] σ_f, MPa	Fracture toughness,[a] MPa $\sqrt{m}$		Elastic modulus, E, GPa		Vickers Microhardness,[a] H, GPa		Density,[a] ρ, g/cm^3	Monoclinic phase, percent
		Mode I, K_{Ic}	Mode II, K_{IIc}	Strain gaging (compression)	Impulse excitation[a]	Indent load=9.8 N	Indent load=19.6 N		
0 (as sprayed)	37.1(3.9)	1.15(0.07)	0.73(0.10)	25	35.1(1.9)	3.31(0.54)	2.36(0.50)	5.147(0.02)	2.533
5	57.3(5.2)	1.83(0.23)	1.30(0.11)	45	68.2(3.5)	5.16(0.77)	4.47(0.83)	5.251(0.016)	2.2
20	87.4(8.4)	2.03(0.15)	1.62(0.17)	55	84.4(0.7)	------------	-----------	-------------	------
100	75.8(7.1)	2.38(0.22)	1.77(0.19)	75	109.6(4.2)	6.46(1.18)	5.00(0.79)	5.275(0.043)	7.7
400	----------	-----------	-----------	---	-----------	------------	-----------	5.230(0.016)	------
500	87.7(10.6)	2.55(0.21)	1.58(0.04)	77	109.6(1.1)	5.79(0.82)	4.34(1.21)	5.213(0.011)	10.46

[a] Numbers in parentheses represent ±1.0 standard deviation.

References

1. Miller, R.A.: Current Status of Thermal Barrier Coatings—An Overview. Surf. Coat. Tech., vol. 30, no. 1, 1987, pp. 1–11.
2. Miller, Robert A., et al.: Thermal Barrier Coatings for Aircraft Engines: History and Directions. Thermal Barrier Coating Workshop, NASA CP–3312, 1995, pp. 17–34.
3. Yonushonis, T.M.: Thick Thermal Barrier Coatings for Diesel Components (Final Report). NASA CR–187111, 1991.
4. Eaton, H.E.; and Novak, R.C.: Sintering Studies of Plasma-Sprayed Zirconia. Surf. Coat. Tech., vol. 32, no. 1–4, 1987, pp. 227–236.
5. Thurn, G., et al.: Toughness Anisotropy and Damage Behavior of Plasma Sprayed ZrO_2 Thermal Barrier Coatings. Surf. Coat. Tech., vol. 123, nos. 2–3, 2000, pp. 147–158.
6. Zhu, Dongming; and Miller, Robert A.: Thermal Conductivity and Elastic Modulus Evolution of Thermal Barrier Coatings Under High Heat Flux Conditions. J. Thermal Spray Tech., vol. 9, no. 2, 2000, pp. 175–180.
7. Thompson, J.A.; and Clyne, T.W.: Effect of Heat Treatment on the Stiffness of Zirconia Top Coats in Plasma-Sprayed TBCs. Acta Materialia, vol. 49, no. 9, 2001, pp. 1565–1575.
8. Steinbrech, R.W.: Thermomechanical Behavior of Plasma Sprayed Thermal Barrier Coatings. Ceram. Eng. Sci. Proc., vol. 23, issues 3–4, 2002, pp. 397–408.
9. Zhu, Dongming; and Miller, Robert A.: Influence of High Cycle Thermal Loads on Thermal Fatigue Behavior of Thick Thermal Barrier Coatings. NASA TP–3676, 1997. http://gltrs.grc.nasa.gov/cgi-bin/GLTRS/browse.pl?1997/TP-3676.html Accessed Oct. 28, 2003.
10. Choi, Sung R.; Zhu, Dongming; and Miller, Robert A.: High-Temperature Slow Crack Growth, Fracture Toughness and Room-Temperature Deformation Behavior of Plasma-Sprayed ZrO_2-8 wt% Y_20_3. Ceram. Eng. Sci. Proc., vol. 19, no. 4, 1998, pp. 293–301.
11. Choi, S.R.; Zhu, D.; and Miller, R.A.: Flexural and Compressive Strengths, and Room-Temperature Creep/Relaxation Properties of Plasma-Sprayed ZrO_2-8 wt% Y_20_3. Ceram. Eng. Sci. Proc., vol. 20, no. 3, 1999, pp. 365–372.

12. Choi, Sung R.; Zhu, Dongming; and Miller, Robert A.: Deformation and Strength Behavior of Plasma-Sprayed ZrO_2 wt% Y_20_3 Thermal Barrier Coatings in Biaxial Flexure and Trans-Thickness Tension. Ceram. Eng. Sci. Proc., vol. 21, no. 4, 2000, pp. 653–661.
13. Choi, S.R.; Zhu, D.; and Miller, R.A.: Deformation and Tensile Cyclic Fatigue of Plasma-Sprayed ZrO_2-8 wt% Y_20_3 Thermal Barrier Coatings. Ceram. Eng. Sci. Proc., vol. 22, issues 3–4, 2001, pp. 427–434.
14. Choi, Sung R.; Zhu, Dongming; and Miller, Robert A.: Mode I, Mode II, and Mixed-Mode Fracture of Plasma-Sprayed Thermal Barrier Coatings at Ambient and Elevated Temperatures. Paper presented at the Eighth International Symposium on Fracture Mechanics of Ceramics (NASA/TM—2003-212185), 2003. http://gltrs.grc.nasa.gov/cgi-bin/GLTRS/browse.pl?2003/TM-2003-212185.html Accessed Oct. 28, 2003.
15. Choi, Sung R.; Zhu, Dongming; and Miller, Robert A.: Strength, Fracture Toughness, Fatigue, and Standardization Issues of Free-Standing Thermal Barrier Coatings. NASA/TM—2003-212516, 2003. http://gltrs.grc.nasa.gov/cgi-bin/GLTRS/browse.pl?2003/TM-2003-212516.html Accessed Oct. 28, 2003.
16. Standard Test Method for Flexural Strength of Advanced Ceramics at Ambient Temperature. Annual Book of ASTM Standards 2003, ASTM Designation: C 1161–02c, section 15, vol. 15.01, ASTM, West Conshohocken, PA, 2003, pp. 223–237.

17a. Kübler, Jakob: Fracture Toughness of Ceramics Using the SEVNB Method—Preliminary Results. Ceram. Eng. Sci. Proc., vol. 18, no. 4, 1997, pp. 155–162.

17b. Kübler, Jakob: Fracture Toughness of Ceramics Using the SEVNB Method; Round Robin. VAMAS Report No. 37, 1999.

18. Standard Test Methods for Determination of Fracture Toughness of Advanced Ceramics at Ambient Temperature. Annual Book of ASTM Standards 2003, ASTM Designation: C 1421–01b, section 15, vol. 15.01, ASTM, West Conshohocken, PA, 2003, pp. 633–666.
19. Suresh, S., et al.: Mixed-Mode Fracture Toughness of Ceramic Materials. J. Am. Ceram. Soc., vol. 73, 1990, pp. 1257–1267.
20. Wang, K.J.; Hsu, C.L.; and Kao, H.: Calculation of Stress Intensity Factors for Combined Mode Bend Specimens. Proceedings of the Fourth International Conference on Fracture, vol. 4, Pergamon Press, New York, NY, 1978, pp. 123–133.
21. He, M.Y.: Asymmetric Four-Point Crack Specimen. J. App. Mech., vol. 67, no. 1, 2000, pp. 207–209.
22. Murakami, Y., et al., eds.: Stress Intensity Factors Handbook. Pergamon, New York, NY, 1987.
23. Srawley, J.E.; and Gross, B.: Side-Cracked Plates Subject to Combined Direct and Bending Forces. ASTM STP 601, 1976, pp. 559–579.
24. Standard Test Method for Dynamic Young’s Modulus, Shear Modulus, and Poisson’s Ratio for Advanced Ceramics by Impulse Excitation of Vibration. Annual Book of ASTM Standards 2003, ASTM Designation: C 1259–01, section 15, vol. 15.01, ASTM, West Conshohocken, PA, 2003, pp. 311–328.
25. Standard Test Method for Vickers Indentation Hardness of Advanced Ceramics. Annual Book of ASTM Standards 2003, ASTM Designation: C 1327–99, section 15, vol. 15.01, ASTM, West Conshohocken, PA, 2003, pp. 468–475.
26. Standard Test Method for Knoop Indentation Hardness of Advanced Ceramics. Annual Book of ASTM Standards 2003, ASTM Designation: C 1326–99, section 15, vol. 15.01, ASTM, West Conshohocken, PA, 2003, pp. 459–466.

27a. Choi, Sung R.; and Bansal, Narottam P.: Strength and Fracture Toughness of YSZ/Alumina Composites for Solid Oxide Fuel Cells. Ceram. Eng. Sci. Proc., vol. 23, issues 3–4, 2002, pp. 741–750.

27b. Choi, Sung R.; and Bansal, Narottam P.: Processing and Mechanical Properties of Various Zirconia/Alumina Composites for Fuel Cell Applications. NASA/TM—2002-211580, 2002.

28. Shetty, D.K.; Rosenfield, A.R.; and Duckworth, W.H.: Mixed-Mode Fracture of Ceramics in Diametral Compression. J. Am. Ceram. Soc., vol. 69, 1986, pp. 437–443.
29. Tikare, Veena; and Choi, Sung R.: Combined Mode I and Mode II Fracture of Monolithic Ceramics. J. Am. Ceram. Soc., vol. 76, no. 9, 1993, pp. 2265–2272.
30. Tikare, Veena; and Choi, Sung R.: Combined Mode I–Mode II Fracture of 12 mol%-Ceria-Doped Tetragonal Zirconia Polycrystalline Ceramic. J. Am. Ceram. Soc., vol. 80, no. 6, 1997, pp. 1624–1626.
31. Choi, Sung R.; and Salem, Jonathan A.: Free-Roller Versus Fixed-Roller Fixtures in Flexure Testing of Advanced Ceramic Materials. Ceram. Eng. Sci. Proc., vol. 17, no. 3, 1996, pp. 69–77.
32. Wesling, K.F.; Socie, D.F.; and Beardsley, B.: Fatigue of Thick Thermal Barrier Coatings. J. Am. Ceram. Soc., vol. 77, no. 7, 1994, pp. 1863–1868.
33. Miller, Robert A.; Leissler, George W.; and Jobe, J. Marcus: Characterization and Durability Testing of Plasma-Sprayed Zirconia-Yttria and Hafnia-Yttria Thermal Barrier Coatings. Part I, NASA TP–3295, 1993.
34. Choi, S.R., et al.: Young's Modulus Strength and Fracture Toughness as a Function of Density of In Situ Toughened Silicon Nitride With 4 wt% Scandia. J. Mater. Sci. Lett., vol. 14, no. 4, 1995, pp. 276–278.
35. Zhu, Dongming; and Miller, Robert A.: Thermal-Barrier Coatings for Advanced Gas-Turbine Engines. MRS Bulletin, vol. 25, no. 7, 2000, pp. 43–47.
36. Zhu, Dongming; and Miller, Robert A.: Thermal Conductivity and Sintering of Advanced Thermal Barrier Coatings. Ceram. Eng. Sci. Proc. (NASA/TM—2002-211481), vol. 23, issues 3–4, 2002, pp. 457–468.
37. Zhu, D., et al.: Furnace Cyclic Behavior of Plasma-Sprayed Zirconia-Yttria and Multi-Component Rare Earth Oxide Doped Thermal Barrier Coatings. Ceram. Eng. Sci. Proc. (NASA/TM—2002-211690), vol. 23, issues 3–4, 2002, pp. 533–545.
38. Zhu, Dongming; Chen, Yuan L.; and Miller, Robert A.: Defect Clustering and Nanophase Structure Characterization of Multicomponent Rare Earth-Oxide-Doped Zirconia-Yttria Thermal Barrier Coatings. NASA/TM—2004-212480, 2004.
39. Moon, Jaeyun, et al.: The Effects of Heat Treatment on the Phase Transformation Behavior of Plasma-Sprayed Stabilized $ZrOr_2$ Coatings. Surf. Coat. Tech., vol. 155, no. 1, 2002, pp. 1–10.

REPORT DOCUMENTATION PAGE

Form Approved
OMB No. 0704-0188

1. AGENCY USE ONLY (*Leave blank*)	**2. REPORT DATE** April 2004	**3. REPORT TYPE AND DATES COVERED** Technical Memorandum

4. TITLE AND SUBTITLE

Effect of Sintering on Mechanical and Physical Properties of Plasma-Sprayed Thermal Barrier Coatings

5. FUNDING NUMBERS

WBS–22–714–30–19

6. AUTHOR(S)

Sung R. Choi, Dongming Zhu, and Robert A. Miller

7. PERFORMING ORGANIZATION NAME(S) AND ADDRESS(ES)

National Aeronautics and Space Administration
John H. Glenn Research Center at Lewis Field
Cleveland, Ohio 44135–3191

8. PERFORMING ORGANIZATION REPORT NUMBER

E–14183

9. SPONSORING/MONITORING AGENCY NAME(S) AND ADDRESS(ES)

National Aeronautics and Space Administration
Washington, DC 20546–0001

10. SPONSORING/MONITORING AGENCY REPORT NUMBER

NASA TM—2004-212625

11. SUPPLEMENTARY NOTES

Portions of this report were presented at the 28th Annual International Conference and Exposition on Advanced Ceramics and Composites sponsored by the American Ceramics Society, Cocoa Beach, Florida, January 25–30, 2004. Sung R. Choi, Ohio Aerospace Institute, Brook Park, Ohio 44142; Dongming Zhu, U.S. Army Research Laboratory, NASA Glenn Research Center; and Robert A. Miller, NASA Glenn Research Center. Responsible person, Sung R. Choi, organization code 5920, 216–433–8366.

12a. DISTRIBUTION/AVAILABILITY STATEMENT

Unclassified - Unlimited
Subject Category: 07 Distribution: Nonstandard

Available electronically at http://gltrs.grc.nasa.gov
This publication is available from the NASA Center for AeroSpace Information, 301–621–0390.

12b. DISTRIBUTION CODE

13. ABSTRACT *(Maximum 200 words)*

The effect of sintering on mechanical and physical properties of free-standing plasma-sprayed ZrO_2-8 wt% Y_2O_3 thermal barrier coatings (TBCs) was determined by annealing them at 1316 °C in air. Mechanical and physical properties of the TBCs, including strength, modes I and II fracture toughness, elastic modulus, Poisson's response, density, microhardness, fractography, and phase stability, were determined at ambient temperature as a function of annealing time ranging from 0 to 500 h. All mechanical and physical properties, except for the amount of monoclinic phase, increased significantly in 5 to 100 h and then reached a plateau above 100 h. Annealing resulted in healing of microcracks and pores and in grain growth, accompanying densification of the TBC's body due to the sintering effect. However, an inevitable adverse effect also occurred such that the desired lower thermal conductivity and good expansivity, which makes the TBCs unique in thermal barrier applications, were degraded upon annealing. A model was proposed to assess and quantify all the property variables in response to annealing in a normalized scheme. Directionality of as-sprayed TBCs appeared to have an insignificant effect on their properties, as determined via fracture toughness, microhardness, and elastic modulus measurements.

14. SUBJECT TERMS

Thermal barrier coatings; Sintering; Sintering effects; Strength; Fracture toughness; Elastic modulus; Density; Hardness; Phase stability

15. NUMBER OF PAGES

32

16. PRICE CODE

17. SECURITY CLASSIFICATION OF REPORT Unclassified	**18. SECURITY CLASSIFICATION OF THIS PAGE** Unclassified	**19. SECURITY CLASSIFICATION OF ABSTRACT** Unclassified	**20. LIMITATION OF ABSTRACT**